Perturbative refinement of the geometric calibration in pinhole SPECT

Michel Defrise[⋆], Christian Vanhove[⋆], Johan Nuyts[‡]

ABSTRACT

The paper investigates the geometric calibration of a rotating gamma camera for pinhole (PH) SPECT imaging. Most calibration methods previously applied in PH-SPECT assume that the motion of the camera around the object belongs to a well defined class described by a small number of geometric parameters, for instance seven parameters for a circular acquisition with a single pinhole camera. The proposed new method refines an initial parametric calibration by applying to each position of the camera a rigid body transformation that is determined to improve the fit between the measured and calculated projections of the calibration sources. A stable estimate of this transformation can be obtained with only three calibration sources by linearizing the equations around the position estimated by the initial parametric calibration. The performance of the method is illustrated using simulated and measured micro-SPECT data.

I. INTRODUCTION

This paper describes a new method for the geometric calibration of a rotating gamma camera for pinhole (PH) SPECT imaging. The method perturbatively refines an initial calibration obtained assuming an ideal, e.g. circular, motion of the gamma camera, and allows to correct small deviations caused by the non perfect mechanical stability of the scanner.

Early works on pinhole SPECT for small animal imaging were based on simple calibration methods which only estimated, often empirically, a few parameters such as the center of rotation, focal length and radius of rotation [1]–[4]. Such techniques are appropriate for clinical SPECT but the magnifying effect of pinhole collimation amplifies the degrading effect on the image of tiny deviations of the parameters from their assumed nominal value. Accurate calibration techniques have since been developed, which led to the exquisite high resolution images which trigger the growing interest for PH-SPECT. Spatial resolutions under 2 mm and even sub-millimetric resolutions have been reported by several groups using different types of single and multiple pinhole collimators [5]–[10] and slit-slat collimators [11]. These systems provide a spectrum of compromises between resolution, sensitivity and size of the field-of-view; see [8] and [12] for recent overviews.

The ultimate approach to calibration consists in exhaustively measuring the response of the scanner to a small radioactive source that is sequentially moved by a robotized system in the center of each image voxel. Pioneered with the FastSPECT scanner [13], this method guarantees optimal image quality by integrating the geometric calibration, the modeling of the pinhole collimator, of the resolution and sensitivity of the detector, and of any other characteristics such a non-linearity of the detector. This gold standard method is time consuming but can be made more efficient by measuring the system response for a smaller set of source locations that appropriately sample the field-of-view and by interpolating the sampled system responses [14], [15]. Even with this improvement this exhaustive calibration method is chiefly aimed at stationary systems and has limited practicability for micro-SPECT systems based on large rotating gamma cameras. One benefit of these systems is the possibility to easily modify the

---

[⋆]Dept. of Nuclear Medicine, Vrije Universiteit Brussel, B-1090 Brussels, Belgium. e-mail: michel.defrise@vub.ac.be, christian.vanhove@az.vub.ac.be. [‡] Dept. of Nuclear Medicine, Katholieke Universiteit Leuven, B-3000 Leuven, Belgium. e-mail: johan.nuyts@uz.kuleuven.ac.be

configuration in function of the object size and shape. This versatility leads to the need for frequent recalibration, ideally before every measurement and at any rate more often than can realistically be achieved with an exhaustive calibration.

Therefore, non-stationnary PH-SPECT systems generally separate the system model into two components: on the one hand a model of the pinhole aperture and camera response, and on the other hand a purely geometric calibration assuming an ideal pinhole system. The former component is based on more or less sophisticated analytic models [16], [17], on Monte-Carlo simulation [18], or again on the measurement of the response to a point source but in this case for a unique reference position of the camera. The present paper deals with the latter component, the *geometric calibration of an ideal pinhole system*, a problem that also arises in SPECT with cone-beam collimators [19], [20], in cone-beam CT [21], [22], and in photogrammetry [23], [24], though with varying practical constraints and accuracy requirements. For a single pinhole camera the goal of the geometric calibration is to determine [20]:

- Three *intrinsic parameters*, for instance the focal length and the two coordinates of the orthogonal projection of the pinhole onto the camera[1]. If the collimator has multiple pinholes, three intrinsic parameters are required for each pinhole. For most scanners the camera-collimator assembly can be considered as rigid and the intrinsic parameters as constant,
- For each position of the camera during a step-and-shoot data acquisition, six *extrinsic parameters*, for instance the 3D location of the pinhole in the laboratory coordinate system, and three angles to determine the orientation of the camera.

The measurement of a calibration phantom with a sufficient number of ”point” sources allows to determine these parameters *independently* for each position of the camera. If six or more point sources with known locations are available, an elegant method [25]–[27] consists in directly estimating the 3×4 homogeneous matrix P that maps the 4 homogeneous coordinates $(x, y, z, 1)$ of a point in the field-of-view onto the 3 homogeneous coordinates $(u, v, 1)$ of its projection on the detector. This representation reduces the calibration problem to the solution of a system of linear equations. An added benefit is that the estimated matrix P can be used directly to implement the forward- and backprojection operations during image reconstruction. The independent calibration of each camera position also has its limitations. First, the number of matrix elements $P_{i,j}$ to be estimated, 12, exceeds the number of independent geometric parameters, 9. Constraints must therefore be introduced to avoid instabilities when solving for P. A second limitation is that the projections of the calibration sources onto the detector must be unambiguously identified, which may be complex to achieve automatically with six or more sources (unless spatially encoded source patterns are used as in [28] for C-arm CT).

The independent calibration of each camera position requires the estimation of a large number of parameters. Even if additional constraints are introduced to enforce the condition that the intrinsic parameters are constant, a total of ($3 + 6\times$number of camera positions) parameters needs to be estimated, making the method sensitive to noise. Better stability, and the possibility to work with fewer point sources, is obtained if the number of calibration parameters is drastically reduced by assuming a simple parametrization of the camera motion during acquisition. This is why the majority of previous papers on PH SPECT calibration assume a perfect rotation of the camera around a fixed axis. The extrinsic calibration then reduces to the estimation of the four parameters required to locate this axis of rotation with respect to some reference frame, defined for instance by the initial position of the camera. Together with the three intrinsic parameters, this leaves a total of only seven calibration parameters[2], which can be estimated from the projections of a small number of non-collinear point sources, as proposed by Hsieh et al [29]–[31]. More recently Bequé et al [32] showed that three non-collinear point sources are necessary, and also sufficient under certain conditions. Note that the spatial location of the calibration phantom

---

[1] We assume throughout the paper that the camera is free of distorsion, the detector pixel size is known, and the two coordinate axes in the detector are orthogonal.

[2] For a single head scanner mounted with a single pinhole collimator. Note that the reference frame can be chosen freely only once. If the scanner has two detector heads, 3 intrinsic parameters and 6 instead of 4 extrinsic parameters are needed for the second head.

must itself be determined, yielding for instance six additional ”nuisance” parameters when using three sources. Algorithms to solve this estimation problem are based either on an analytic solution [22], [33] or on the optimization of a cost function [19], [29]–[32] that quantifies the goodness of fit between the measured and estimated projections of the sources for the complete set of camera positions. The accuracy of the estimation is sometimes hampered by correlations among some of the 7 parameters. This problem has been addressed by a priori fixing some of the parameters, by restricting the search domain during optimization [33], [35], [36], or by separately estimating the intrinsic and the extrinsic parameters [20]. In this work we use the optimization method of Bequé et al [32], which allows an arbitrary parametrization of the orbit and hence can be applied directly for a helical orbit [36], [37], or for a scanner with more than one head and with multiple pinhole collimators. This method has been extensively validated [38], [39] and has recently been implemented using homogeneous coordinates [37].

The excellent image quality obtained by many groups assuming an ideal rotation of the camera demonstrates the good mechanical accuracy and stability of scanners that were originally designed for low resolution clinical applications of SPECT rather than for the high resolution imaging of small laboratory animals. Nevertheless, stability is not perfect and small deviations have been reported [36], [40], [42], the effect of which is amplified by the large magnification of the pinhole geometry. In one example [42] the tilt angle of the camera was observed to vary as the camera rotates around the object. Despite a small amplitude of only about 0.3 degrees, this oscillation caused a significant degradation of image quality when pure rotational motion was assumed during image reconstruction. Once parametrized as a sinusoidal variation of the tilt angle, it was possible to quantify and correct this oscillation using Bequé’s method. Unfortunately, it is in general difficult to propose an adequate parametrization for a small unknown and irregular displacement of the camera.

Building on methods applied in photogrammetry [24] this paper proposes an improved calibration method which, starting from an initial calibration based on a parametric model of the camera motion, refines the extrinsic parameters *of each camera position independently* by applying to the camera a small rotation and translation calculated to improve the fit between the observed and estimated projections of the calibration sources. The method only requires three ”point” sources and can therefore be applied using the same calibration measurements as those collected for the initial calibration. Its computational cost is negligible and it can be applied independently of the nature of the orbit assumed by the initial calibration and of the specific algorithm used for this initial calibration. The major limitation is the requirement that the initial parametric calibration be sufficiently accurate to guarantee that the corrective displacement of the detector remains small. This condition is easy to check when applying the method and is usually satisfied in practice. Results with a single pinhole collimator on the Siemens dual-head gamma camera (e.cam, Siemens, Hoffman Estates, Ill.) demonstrate that the deviations of the camera from its circular motion are reproducible and that even tiny corrections to the initial calibration result in visible, though marginal, improvements of image quality.

In section II we introduce notations and define the calibration problem. We show how the assumption that the correcting motion is small (mathematically: infinitesimal) linearizes the problem and reduces it to the solution of a set of linear equations. That system of equations is solved using a truncated singular value decomposition (SVD) to avoid potential ill-conditioning. Implementation details will be given before presenting in section III a validation on simulated and measured micro-SPECT data.

II. A REFINED CALIBRATION METHOD

A. An initial parametric calibration

To simplify the presentation we consider first a single head gamma camera equipped with a single pinhole collimator; generalizations will be discussed in section II.E. Cartesian detector coordinates (u, v) are defined with respect to two orthonormal axes with known pixel size. A calibration phantom consisting of $n \geq 3$ sources $i = 1, \cdots, n$ is measured for M orbit positions $\alpha = 1, \cdots, M$ of the camera. For each position of the camera the center of mass of the measured projection of each source is calculated, yielding the *calibration data*

$$(u_{i,\alpha}^{obs}, v_{i,\alpha}^{obs}) \quad i = 1, \cdots, n, \ \alpha = 1, \cdots, M \tag{1}$$

Because of the diverging geometry of the pinhole collimator, the maximum diameter of the calibration sources should be sufficiently small to ensure that the distance between the center of mass of the projection of a source, and the projection of its 3D center of mass is negligible.

We assume that the calibration data (1) have been fit by a parametric model of the expected nominal orbit of the camera around the object. This model depends on a small number of parameters, for instance 7 for a single pinhole collimator and a circular orbit. These parameters are estimated using some analytic or optimization technique and the resulting *initial calibration* of the pinhole system is our starting point. The nature of the orbit model, the number of its parameters, and the specific calibration algorithm used are irrelevant for the rest of this section.

From the output of the initial calibration we can calculate the following quantities, which fully characterize the acquisition geometry and are sufficient for image reconstruction:

- *The nuisance parameters*: the positions of the point sources $\vec{x}_i \in \mathbb{R}^3, i = 1, \cdots, n$.
- *The three intrinsic parameters*:
  1) The focal length F,
  2) The detector coordinates (m_u, m_v) of the orthogonal projection $\vec{c}_\alpha \in \mathbb{R}^3$ of the pinhole aperture onto the detector,
- *The extrinsic parameters* specify for each position $\alpha = 1, \cdots, M$ the position and orientation of the camera with respect to some fixed reference frame linked e.g. to the gantry (figure 1):
  1) The pinhole aperture $\vec{f}_\alpha \in \mathbb{R}^3$,
  2) The orthogonal projection $\vec{c}_\alpha \in \mathbb{R}^3$ of the pinhole aperture $\vec{f}_\alpha$ onto the detector,
  3) Two orthonormal vectors $\vec{e}_{u,\alpha}$ and $\vec{e}_{v,\alpha} \in \mathbb{R}^3$ which define the coordinate axes in the detector plane.

To simplify notations we assume below that the coordinates u, v have been shifted in such a way that the detector pixel $u = 0, v = 0$ coincides with $\vec{c}_\alpha$. This shift can be achieved using the estimated intrinsic parameters m_u and m_v. The extrinsic parameters satisfy the following six constraints[3]

$$\begin{array}{lll} ||\vec{c}_\alpha - \vec{f}_\alpha|| = F & ||\vec{e}_{u,\alpha}|| = 1 & ||\vec{e}_{v,\alpha}|| = 1 \\ \vec{e}_{u,\alpha} \cdot (\vec{c}_\alpha - \vec{f}_\alpha) = 0 & \vec{e}_{v,\alpha} \cdot (\vec{c}_\alpha - \vec{f}_\alpha) = 0 & \vec{e}_{u,\alpha} \cdot \vec{e}_{v,\alpha} = 0 \end{array} \quad \alpha = 1, \cdots, M \tag{2}$$

where $\vec{a} \cdot \vec{b}$ denotes the cartesian scalar product in $\mathbb{R}^3$ and $||\vec{a}|| = \sqrt{\vec{a} \cdot \vec{a}}$.

Using the initial calibration we can calculate for each α the expected projections of the n point sources as

$$u_{i,\alpha}^{cal} = \frac{F^2 \, \vec{e}_{u,\alpha} \cdot (\vec{x}_i - \vec{f}_\alpha)}{(\vec{c}_\alpha - \vec{f}_\alpha) \cdot (\vec{x}_i - \vec{f}_\alpha)} \text{ and } v_{i,\alpha}^{cal} = \frac{F^2 \, \vec{e}_{v,\alpha} \cdot (\vec{x}_i - \vec{f}_\alpha)}{(\vec{c}_\alpha - \vec{f}_\alpha) \cdot (\vec{x}_i - \vec{f}_\alpha)} \quad i = 1, \cdots, n, \ \alpha = 1, \cdots, M \tag{3}$$

Equation (3) can be expressed equivalently using the 3×4 projection matrices in homogeneous coordinates,

$$P_\alpha = \begin{pmatrix} F^2(\vec{e}_{u,\alpha})_x & F^2(\vec{e}_{u,\alpha})_y & F^2(\vec{e}_{u,\alpha})_z & -F^2\vec{e}_{u,\alpha} \cdot \vec{f}_\alpha \\ F^2(\vec{e}_{v,\alpha})_x & F^2(\vec{e}_{v,\alpha})_y & F^2(\vec{e}_{v,\alpha})_z & -F^2\vec{e}_{v,\alpha} \cdot \vec{f}_\alpha \\ (\vec{c}_\alpha - \vec{f}_\alpha)_x & (\vec{c}_\alpha - \vec{f}_\alpha)_y & (\vec{c}_\alpha - \vec{f}_\alpha)_z & -(\vec{c}_\alpha - \vec{f}_\alpha) \cdot \vec{f}_\alpha \end{pmatrix} \quad \alpha = 1, \cdots, M \tag{4}$$

The accuracy of the calibration can be characterized by the magnitudes $|u_{i,\alpha}^{obs} - u_{i,\alpha}^{cal}|$ and $|v_{i,\alpha}^{obs} - v_{i,\alpha}^{cal}|$ of the deviations between the measured and calculated detector coordinates. These deviations may be caused by the errors in the calibration data $(u_{i,\alpha}^{obs}, v_{i,\alpha}^{obs})$ or by the calibration algorithm being trapped in a

---

[3] There are 6 scalar constraints in (2). Subtracting this from the 12 scalars needed for the four vectors $\vec{f}_\alpha, \vec{c}_\alpha, \vec{e}_{u,\alpha}, \vec{e}_{v,\alpha}$ there remains 6 independent extrinsic parameters for each camera position, as was noted in the introduction.

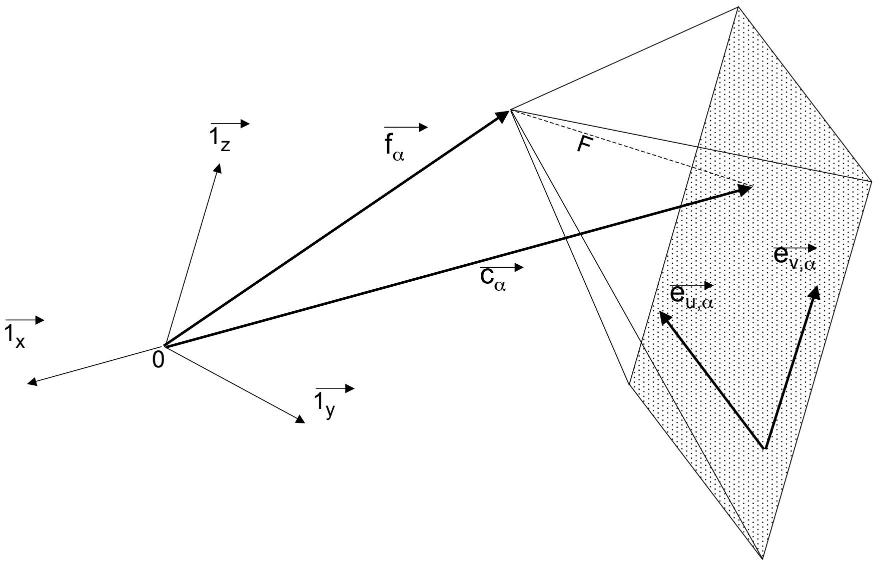

Fig. 1. Definition of the extrinsic parameters for a plane detector (colored pattern) with a pyramidal single pinhole collimator. The vector $\vec{f}_\alpha$ defines the position of the pinhole aperture in a fixed reference frame $(0, \vec{1}_x, \vec{1}_y, \vec{1}_z)$. The vector $\vec{c}_\alpha$ defines the position of the orthogonal projection of the pinhole aperture on the detector plane. The orthogonal unit vectors $\vec{e}_{u,\alpha}$ and $\vec{e}_{v,\alpha}$ define the cartesian coordinate system in the detector plane.

local minimum of the cost function. Deviations, however, also arise when the actual motion of the camera does not belong to the class of orbits described by the parametrization selected for the initial calibration. In that case, the orbit model cannot accurately fit the calibration data and the deviations $|u^{obs}_{i,\alpha} - u^{cal}_{i,\alpha}|$ and $|v^{obs}_{i,\alpha} - v^{cal}_{i,\alpha}|$ may significantly deviate from zero. This leads to suboptimal image reconstructions. The goal of this paper is to correct these residual deviations.

B. Perturbative correction of the initial calibration

We estimate in this section improved values of the extrinsic parameters $\vec{f}_\alpha, \vec{c}_\alpha, \vec{e}_{u,\alpha}, \vec{e}_{v,\alpha}$ using the following hypotheses:

- The assembly camera/collimator is rigid and the errors in the three *intrinsic parameters* F, m_u and m_v estimated by the initial calibration can be neglected,
- The initial calibration is accurate in the sense that the discrepancies $|u^{obs}_{i,\alpha} - u^{cal}_{i,\alpha}|$ and $|v^{obs}_{i,\alpha} - v^{cal}_{i,\alpha}|$ are ”small” in some sense defined below,
- The discrepancies are at least partly caused by *reproducible* deviations of the camera motion from the assumed parametric model,
- The errors in the positions $\vec{x}_i \in \mathbb{R}^3$ of the n point sources estimated by the initial calibration can be neglected.

The last hypothesis can be replaced by the weaker hypothesis that the difference between the estimated and true positions of the point sources is equivalent to a rigid body transformation. This weaker condition is automatically satisfied if the initial calibration algorithm uses as prior knowledge an accurate measurement of the relative positions of the point sources in the phantom, as in [32].

Under the above hypotheses, the extrinsic parameters of each position of the camera can be corrected by applying to the camera a rigid body transformation represented by a ”small” translation

$\vec{t}_\alpha \in \mathbb{R}^3$ and a "small" rotation of angle θ_α around an axis defined by a unit vector $\vec{n}_\alpha$. "Small" here means that calculations can be limited to the first order in $||\vec{t}_\alpha||/F$ and in θ_α, using relations of the type $\sin\theta_\alpha \simeq \theta_\alpha$.

The rigid body transformation will be determined *independently for each camera position*. Therefore we will work in the rest of this section with a fixed camera position α, and will omit this index α to simplify notations. The corrected parameters will be denoted by a $'$:

$$\begin{aligned}
\vec{e}'_u &= \vec{e}_u + \vec{\theta} \times \vec{e}_u \\
\vec{e}'_v &= \vec{e}_v + \vec{\theta} \times \vec{e}_v \\
\vec{f}' &= \vec{f} + \vec{t} + \vec{\theta} \times \vec{f} \\
\vec{c}' &= \vec{c} + \vec{t} + \vec{\theta} \times \vec{c}
\end{aligned} \tag{5}$$

where $\vec{\theta} = \theta\,\vec{n}$ and $\vec{a} \times \vec{b}$ is the vector product (cross product) of two vectors $\vec{a}, \vec{b} \in \mathbb{R}^3$. The mapping $\vec{a} \rightarrow \vec{a} + \vec{\theta} \times \vec{a}$ represents an infinitesimal rotation of angle θ around an axis $\vec{n}$ (see e.g. [44]). The corrected parameters in equation (5) satisfy to the first order in $||\vec{t}||$ and θ the same constraints (2) as the original parameters, e.g. $||\vec{c}' - \vec{f}'|| = ||\vec{c} - \vec{f}|| = F$. This can be verified using standard properties of the vector product, such as $\vec{a} \cdot (\vec{b} \times \vec{a}) = 0$ and $\vec{a} \cdot (\vec{b} \times \vec{c}) = \vec{c} \cdot (\vec{a} \times \vec{b}) = -\vec{c} \cdot (\vec{b} \times \vec{a})$.

With the corrected parameters defined by (5) the estimated projections of the point sources become (recall that all u and v variables have been shifted so that $m_u = m_v = 0$):

$$u_i'^{cal} = \frac{F^2\,\vec{e}'_u \cdot (\vec{x}_i - \vec{f}')}{(\vec{c}' - \vec{f}') \cdot (\vec{x}_i - \vec{f}')} \text{ and } v_i'^{cal} = \frac{F^2\,\vec{e}'_v \cdot (\vec{x}_i - \vec{f}')}{(\vec{c}' - \vec{f}') \cdot (\vec{x}_i - \vec{f}')} \quad i = 1, \cdots, n \tag{6}$$

and the aim is to make this as close as possible to the calibration data $(u_i^{obs}, v_i^{obs}), i = 1, \cdots, n$. In the next subsection we determine a rigid body transformation of the camera that minimizes the residual error

$$E^2 = \sum_{i=1}^{n} \left(|u_i'^{cal} - u_i^{obs}|^2 + |v_i'^{cal} - v_i^{obs}|^2 \right) \tag{7}$$

We do not here consider alternative cost functions which could provide a better robustness to outliers (aberrant values of u_i^{obs} or v_i^{obs}) than the gaussian noise model implicit in equation (7). See for instance [24].

C. Calculation of the rigid body transformation for one camera position

As above, we consider a fixed camera position and drop the index α. Inserting (5) into (6) we obtain

$$u_i'^{cal} = \frac{F^2\,\vec{e}_u \cdot (\vec{x}_i - \vec{f}) + F^2(\vec{\theta} \times \vec{e}_u) \cdot (\vec{x}_i - \vec{f}) - F^2 \vec{e}_u \cdot (\vec{t} + \vec{\theta} \times \vec{f}) + O(t\theta, \theta^2)}{(\vec{c} - \vec{f}) \cdot (\vec{x}_i - \vec{f}) - (\vec{t} + \vec{\theta} \times \vec{f}) \cdot (\vec{c} - \vec{f}) + (\vec{x}_i - \vec{f}) \cdot [\vec{\theta} \times (\vec{c} - \vec{f})] + O(t\theta, \theta^2)} \quad i = 1, \cdots, n \tag{8}$$

with a similar equation for $v_i'^{cal}$. The notation $O(t\theta, \theta^2)$ denotes terms of higher order that will be neglected because we assume that the correction to the initial calibration is small. Note that two terms in the numerator of (8) cancel because $(\vec{\theta} \times \vec{e}_u) \cdot \vec{f} = -\vec{e}_u \cdot (\vec{\theta} \times \vec{f})$. Likewise, two terms cancel in the denominator because $(\vec{\theta} \times \vec{f}) \cdot (\vec{c} - \vec{f}) = -\vec{f} \cdot [\vec{\theta} \times (\vec{c} - \vec{f})]$. With these cancellations equation (8) simplifies as

$$u_i'^{cal} = \frac{F^2\,\vec{e}_u \cdot (\vec{x}_i - \vec{f}) + F^2(\vec{\theta} \times \vec{e}_u) \cdot \vec{x}_i - F^2 \vec{e}_u \cdot \vec{t} + O(t\theta, \theta^2)}{(\vec{c} - \vec{f}) \cdot (\vec{x}_i - \vec{f}) - \vec{t} \cdot (\vec{c} - \vec{f}) + \vec{x}_i \cdot [\vec{\theta} \times (\vec{c} - \vec{f})] + O(t\theta, \theta^2)} \tag{9}$$

Using $(A + \epsilon)/(B + \epsilon') = A/B + (\epsilon - (A/B)\epsilon')/B + O(\epsilon'^2, \epsilon\epsilon')$ and recalling equation (3), this becomes,

$$\begin{aligned}
u_i'^{cal} &= u_i^{cal} + \frac{F^2(\vec{\theta} \times \vec{e}_u) \cdot \vec{x}_i - F^2 \vec{e}_u \cdot \vec{t} + u_i^{cal}\vec{t} \cdot (\vec{c} - \vec{f}) - u_i^{cal}\vec{x}_i \cdot [\vec{\theta} \times (\vec{c} - \vec{f})]}{(\vec{c} - \vec{f}) \cdot (\vec{x}_i - \vec{f})} + O(t^2, t\theta, \theta^2) \\
&= u_i^{cal} + \vec{t} \cdot \vec{U}_i + \vec{\theta} \cdot (\vec{x}_i \times \vec{U}_i) + O(t^2, t\theta, \theta^2) \quad i = 1, \cdots, n
\end{aligned} \tag{10}$$

where we have defined the vectors

$$\vec{U}_i = \frac{-F^2\vec{e}_u + u_i^{cal}(\vec{c}-\vec{f})}{(\vec{c}-\vec{f})\cdot(\vec{x}_i-\vec{f})} \quad i = 1, \cdots, n \tag{11}$$

Similar expressions hold for the v coordinates:

$$v_i'^{cal} = v_i^{cal} + \vec{t}\cdot\vec{V}_i + \vec{\theta}\cdot(\vec{x}_i \times \vec{V}_i) + O(t^2, t\theta, \theta^2) \quad i = 1, \cdots, n \tag{12}$$

with

$$\vec{V}_i = \frac{-F^2\vec{e}_v + v_i^{cal}(\vec{c}-\vec{f})}{(\vec{c}-\vec{f})\cdot(\vec{x}_i-\vec{f})} \quad i = 1, \cdots, n \tag{13}$$

The vectors $\vec{U}_i$ and $\vec{V}_i$ can be calculated for the n sources using the result of the initial calibration. To estimate the 6 parameters $\vec{t}, \vec{\theta}$ of the rigid body transformation that must be applied to the detector, we drop the terms in $O(t^2, t\theta, \theta^2)$ in equations (10) and (12) and solve the $2n$ linear equations

$$\begin{array}{lll} u_i^{obs} = u_i'^{cal} & \Leftrightarrow & u_i^{obs} - u_i^{cal} = \vec{t}\cdot\vec{U}_i + \vec{\theta}\cdot(\vec{x}_i \times \vec{U}_i) \quad i = 1, \cdots, n \\ v_i^{obs} = v_i'^{cal} & \Leftrightarrow & v_i^{obs} - v_i^{cal} = \vec{t}\cdot\vec{V}_i + \vec{\theta}\cdot(\vec{x}_i \times \vec{V}_i) \quad i = 1, \cdots, n \end{array} \tag{14}$$

for $\vec{t}$ and $\vec{\theta}$. These equations can be written in matrix notations as $d = \mathcal{M}\cdot T$, with $d \in \mathbb{R}^{2n}$, $\mathcal{M} \in \mathbb{R}^{2n\times 6}$ and $T \in \mathbb{R}^6$:

$$\begin{pmatrix} d_1 = u_1^{obs} - u_1^{cal} \\ d_2 = u_2^{obs} - u_2^{cal} \\ \cdots \\ d_n = u_n^{obs} - u_n^{cal} \\ d_{n+1} = v_1^{obs} - v_1^{cal} \\ d_{n+2} = v_2^{obs} - v_2^{cal} \\ \cdots \\ d_{2n} = v_n^{obs} - v_n^{cal} \end{pmatrix} = \begin{pmatrix} \vec{U}_{1,x} & \vec{U}_{1,y} & \vec{U}_{1,z} & (\vec{x}_1 \times \vec{U}_1)_x & (\vec{x}_1 \times \vec{U}_1)_y & (\vec{x}_1 \times \vec{U}_1)_z \\ \vec{U}_{2,x} & \vec{U}_{2,y} & \vec{U}_{2,z} & (\vec{x}_2 \times \vec{U}_2)_x & (\vec{x}_2 \times \vec{U}_2)_y & (\vec{x}_2 \times \vec{U}_2)_z \\ \cdots \\ \vec{U}_{n,x} & \vec{U}_{n,y} & \vec{U}_{n,z} & (\vec{x}_n \times \vec{U}_n)_x & (\vec{x}_n \times \vec{U}_n)_y & (\vec{x}_n \times \vec{U}_n)_z \\ \vec{V}_{1,x} & \vec{V}_{1,y} & \vec{V}_{1,z} & (\vec{x}_1 \times \vec{V}_1)_x & (\vec{x}_1 \times \vec{V}_1)_y & (\vec{x}_1 \times \vec{V}_1)_z \\ \vec{V}_{2,x} & \vec{V}_{2,y} & \vec{V}_{2,z} & (\vec{x}_2 \times \vec{V}_2)_x & (\vec{x}_2 \times \vec{V}_2)_y & (\vec{x}_2 \times \vec{V}_2)_z \\ \cdots \\ \vec{V}_{n,x} & \vec{V}_{n,y} & \vec{V}_{n,z} & (\vec{x}_n \times \vec{V}_n)_x & (\vec{x}_n \times \vec{V}_n)_y & (\vec{x}_n \times \vec{V}_n)_z \end{pmatrix} \begin{pmatrix} t_x \\ t_y \\ t_z \\ \theta_x \\ \theta_y \\ \theta_z \end{pmatrix} \tag{15}$$

In practice, the system of equations is modified to obtain consistent units: the first three columns of $\mathcal{M}$ are multiplied by the focal length F (or another fixed length of similar magnitude) while the three first components of the parameter vector T are divided by F. We nevertheless keep the simpler expression (15) to avoid overloading notations.

D. Implementation.

The system of linear equations (15) does not guarantee existence or uniqueness of the solution. A necessary condition for uniqueness is that the calibration phantom has a least three sources, but this condition is not sufficient since even with $n \geq 3$ the system can be singular or quasi-singular (i.e. ill-conditionned) for some exceptional configurations. The matrix $\mathcal{M}$ is always singular, for instance, when the sources are collinear. In addition, the system is overdetermined if $n > 3$, and in that case does not in general admit a solution at all.

To overcome these well-known difficulties, we calculate the singular value decomposition (SVD) of the $2n \times 6$ matrix $\mathcal{M}$ as (see e.g. [45])

$$\mathcal{M} = G \cdot W \cdot H^t \tag{16}$$

where

- G is a $2n \times 6$ matrix, the columns of which define 6 orthonormal *singular vectors* $g_k \in \mathbb{R}^{2n}$, with $G_{i,k} = (g_k)_i$ for $k = 1, \cdots, 6$ and $i = 1, \cdots, 2n$.
- H is a 6×6 matrix, the columns of which define 6 orthonormal *singular vectors* $h_k \in \mathbb{R}^6$, with $H_{j,k} = (h_k)_j$ for $j, k = 1, \cdots, 6$

- W is a 6×6 diagonal matrix $W_{k',k} = \sigma_k \, \delta_{k',k}$ where the *singular values* $\sigma_k \geq 0, k = 1, \cdots, 6$ are conventionally sorted by decreasing magnitudes as $\sigma_1 \geq \sigma_2 \geq \cdots \sigma_6 \geq 0$.
- Each singular component $k = 1, \cdots, 6$ satisfies $\mathcal{M} h_k = \sigma_k \, g_k$ and $\mathcal{M}^t g_k = \sigma_k \, h_k$.

We then define an approached, regularized, solution of (15) as a truncated SVD solution

$$(t_x, t_y, t_z, \theta_x, \theta_y, \theta_z)^t = T^{(\epsilon)} = \sum_{k=1, \sigma_k > \epsilon \sigma_1}^{6} \frac{1}{\sigma_k} \left(g_k^t \cdot d \right) \, h_k \tag{17}$$

where σ_1 is the largest singular value of $\mathcal{M}$ and $g_k^t \cdot d$ denotes the cartesian scalar product in $\mathbb{R}^{2n}$. The small regularization parameter $0 \leq \epsilon \leq 1$ is chosen empirically in function of the expected accuracy of the calibration data (we use $\epsilon = 0.02$ in section III). When $\epsilon = 0$, $T^{(\epsilon)}$ is the generalized (Moore-Penrose) solution of (15), which is the solution of minimum norm that minimizes the residual error E^2 [45].

Recall that we have so far considered a single camera position α and have omitted this index to simplify notations. In practice the system (15) is built, then solved using (17), *independently* for each camera position $\alpha = 1, \cdots, M$. Reintroducing this index the overall result of the refined calibration is a set of estimated translations $\vec{t}_\alpha$ and rotations $\vec{\theta}_\alpha$. Inserting these into equations (5) yields the new extrinsic parameters $\vec{c}'_\alpha, \vec{f}'_\alpha, \vec{e}'_{u,\alpha}, \vec{e}'_{v,\alpha}$ of the pinhole system. As was already noted below equation (5), these modified vectors satisfy the constraints (2) only to first order in θ_α. Therefore, after calculating (5) orthonormalisation is applied to exactly enforce the constraints (2).

Although noise is controlled by the regularization parameter ϵ in equation (17), additional regularization may optionally be applied by post-smoothing each component of the rigid body transform $T_\alpha^{(\epsilon)} \in \mathbb{R}^6$ with a low-pass filter in the α index, defined by some smoothing kernel w_α:

$$T_{\alpha,j}^{(\epsilon)} \leftarrow \sum_{\alpha'=1}^{M} w_{\alpha-\alpha'} \, T_{\alpha',j}^{(\epsilon)} \quad \alpha = 1, \cdots, M, \; j = 1, \cdots, 6 \tag{18}$$

This low-pass filter avoids overfitting non-reproducible noisy deviations $|u_{i,\alpha}^{obs} - u_{i,\alpha}^{cal}|$ and $|v_{i,\alpha}^{obs} - v_{i,\alpha}^{cal}|$ between the measured and initially calculated calibration data. Filtering however could also smooth out an actual discontinuous displacement of the camera, which would otherwise have been modelled and corrected. In such a case, beter results might be obtained using a median filter instead of the linear filter (18). No post-smoothing was applied to the data in section III.

E. Generalizations

The refinement method is applicable without change to a scanner with multiple heads, each mounted with a single pinhole collimator. In this case the rigid body transformation $\vec{t}_\alpha, \vec{\theta}_\alpha$ is estimated independently for each head to allow modelling a non-perfect rigidity of the multiple head assembly. The situation is different when calibrating a collimator with P pinhole apertures: one can usually assume that the collimator does not undergo any deformation during the motion of the camera, and therefore, a unique rigid body transformation $\vec{t}_\alpha, \vec{\theta}_\alpha$ must be estimated for each position α of the scanner, and applied to all pinhole apertures. The transformation is defined by a regularized solution of the system of $2nP$ equations for the same 6 unknowns as before, obtained by concatenating P systems like (15).

III. RESULTS

A. Data acquisition

The calibration method has been evaluated using measured and simulated data for a Siemens dual-head gamma camera (e.cam, Siemens, Hoffman Estates, Ill.). Each head is equipped with a single pinhole collimator (Nuclear Fields, Vortum-Mullem, Netherlands), with a tungsten aperture of 1.5 mm or 1.0 mm diameter. The major applications of this system concern gated cardiac studies and the study of tumor xenografts on rats and mice.

Calibration data were measured with three sources obtained by filling with $100\mu Ci/\mu L$ ^{99m}Tc three cylindrical holes of about 1 mm diameter and 1 mm length drilled into a 4 mm thick sheet of plexiglas. The three sources form a triangle with sides 25.5 mm, 19.0 mm and 26.0 mm. Projections were acquired for $M = 64$ positions of the camera, which were (nominally) uniformly spaced over 360 degrees. For each projection $\alpha = 1, \cdots, M$ the coordinates $(u^{obs}_{i,\alpha}, v^{obs}_{i,\alpha})$ of the projection of the three sources $i = 1, 2, 3$ were estimated automatically as follows. First, the coordinates of the three largest local maxima in the projection image are determined. These maxima correspond approximately to the position of the three calibration sources on the detector surface. Next, a more precise localization of the projection of each source is obtained as the count based weighted average of all connected detector pixels that have a count density larger than 50% of the corresponding local maximum.

B. Simulation study

The accuracy and robustness of the proposed calibration method have been evaluated with simulated calibration data for the e.cam scanner, with a pinhole diameter of 1.5 mm and a projection matrix size of 128×128 with a pixel of 4.8 mm. An initial calibration assuming a perfect circular acquisition was done using Bequé's method, and yielded a focal length $F = 280$ mm and a distance between the pinhole aperture and the axis of rotation $ROR = 46$ mm. With these parameters and the intrinsic resolution of 3.8 mm for the e.cam detector, the standard approximate expression for the spatial resolution of a pinhole system [12] predicts a resolution of about 1.9 mm. After multiplication by the magnification factor F/ROR, this translates into a resolution of 11.3 mm in the detector, indicating that the chosen detector pixel size of 4.8 mm satisfies the condition for aliasing-free sampling.

Non-ideal acquisition geometries were simulated by perturbing this ideal circular acquisition. The calibration parameters $\vec{f}_\alpha, \vec{c}_\alpha, \vec{e}_{u,\alpha}, \vec{e}_{v,\alpha}$ for the non-ideal geometry were generated by applying for each position $\alpha = 1, \cdots, M$ of the camera a translation $\vec{t}_\alpha$ and rotation $\vec{\theta}_\alpha = \theta_\alpha \, \vec{n}_\alpha$ to the assembly detector/collimator. The origin of the reference frame is located at the center of the field-of-view. The rotation and translation vectors were determined randomly, according to

$$\begin{aligned}
(\vec{\theta}_\alpha)_j &= \sum_{k=1}^{4} \frac{\theta_a}{k^2} \left(A_{k,j} \cos \frac{2\pi\alpha}{M} + B_{k,j} \sin \frac{2\pi\alpha}{M} \right) \\
(\vec{t}_\alpha)_j &= \sum_{k=1}^{4} \frac{t_a}{k^2} \left(C_{k,j} \cos \frac{2\pi\alpha}{M} + D_{k,j} \sin \frac{2\pi\alpha}{M} \right) \qquad (19)
\end{aligned}$$

where $j = 1, 2, 3$ for the three cartesian components of the vectors and $A_{k,j}, B_{k,j}, C_{k,j}, D_{k,j}$ are independent normally distributed pseudo-random numbers (mean 0, standard deviation 1). The parameters t_a and θ_a allow to tune the amplitude of the simulated deviations from the ideal circular orbit, and the factor $1/k^2$ is introduced to mimic a typical decay of Fourier coefficients with increasing frequency k. Note that the assembly detector/collimator was rotated using the actual rotation matrix defined by $\vec{\theta}_\alpha = \theta_\alpha \, \vec{n}_\alpha$, rather than the small angle approximation (5) that was used to derive the proposed method.

For each non-ideal geometry generated according to (19), the "exact" projections $u^{exact}_{i,\alpha}$ and $v^{exact}_{i,\alpha}$, $i = 1, 2, 3$ and $\alpha = 1, \cdots, 64$ of the calibration sources were calculated according to equation (3). Gaussian noise with standard deviation $\sigma = 1.0$ mm was then added to obtain simulated calibration data $u^{obs}_{i,\alpha}$ and $v^{obs}_{i,\alpha}$. A total of 110 geometries were simulated with various combinations of the translation and rotation magnitudes in equation (19), ranging from 0.5 to 3 mm for the translation t_a and from 0.5 to 5 degrees for the rotation θ_a. The simulated calibration data were first processed assuming an ideal circular orbit (Bequé's method), and then refined as described in section II.

For each method and for each of the 110 simulations we calculated the root-mean-square error

$$< E >= \sqrt{\frac{1}{3 \times 64} \sum_{i=1}^{3} \sum_{\alpha=1}^{64} \left(|u^{cal}_{i,\alpha} - u^{exact}_{i,\alpha}|^2 + |v^{cal}_{i,\alpha} - v^{exact}_{i,\alpha}|^2 \right)} \qquad (20)$$

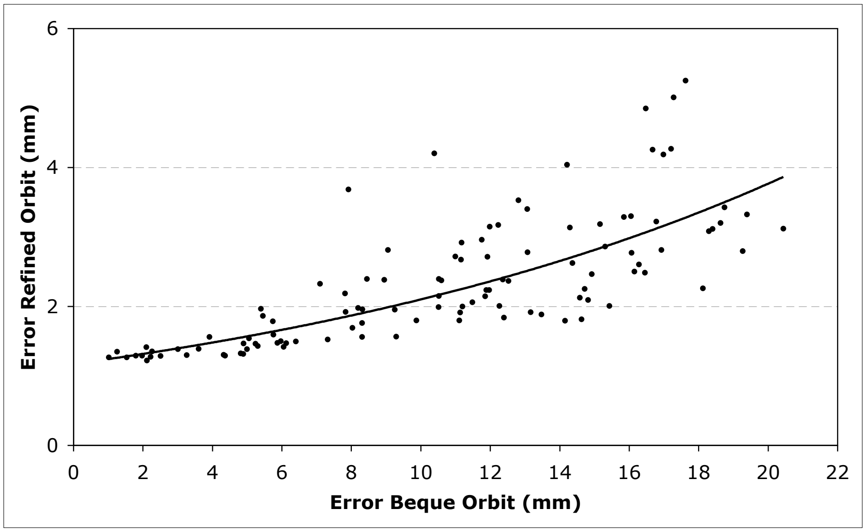

Fig. 2. Root-mean-square error E (equation (20)) between the exact and the calculated coordinates of the projections of the calibration sources. The error is averaged over the 64 camera positions and over the three sources. Each symbol corresponds to one simulated non-ideal acquisition geometry, and the increasing errors correspond to simulations with increasing values of the simulated deviations from a circular motion. The detector pixel size is 4.8 mm. Vertical axis: error with the refined method. Horizontal axis: error with an initial calibration that assumes a perfect circular motion of the camera. The line is a least-square fit with a second order polynomial.

where $u_{i,\alpha}^{cal}$ and $v_{i,\alpha}^{cal}$ are the projections of the three sources calculated using the chosen calibration method. Figure 2 shows the root-mean-square error $< E >$ with the refined method plotted versus $< E >$ with the initial calibration. Note that the two axis in figure 2 represent lengths in the detector plane, as in equation (20). These lengths should be demagnified by an average factor $F/ROR \simeq 6$ to be interpreted in image space.

C. Reproducibility with measured data

The statistical errors on the calibration data were estimated by acquiring 10 successive calibration scans of 900 s on the e.cam, with a pinhole diameter of 1.5 mm and a projection matrix size of 256×256 with a pixel of 2.4 mm. For each scan the coordinates $(u_{i,\alpha}^{obs}, v_{i,\alpha}^{obs})$ were determined as described in section III.A, and the standard deviation of the 10 estimates were calculated. The average standard deviation on $u_{i,\alpha}^{obs}$ and $v_{i,\alpha}^{obs}$ was $\sigma = 0.48$ mm.

Figure 3 shows the angular variations of the three components of the translation and rotation vectors estimated from the ten successive calibration scans acquired with the e.cam system. Clearly, it would be difficult to define an appropriate parametrization for these irregularly varying quantities, and the fact that the proposed method does not require any specific model for the camera motion is an important advantage. The magnitude of the errors indicates the good numerical stability of the method and the fact that the deviations from an ideal circular motion are fairly reproducible with this scanner. Comparison with the results for a second series of ten calibration scans taken one month later, with a different position of the calibration sources, shows that the major features of the motion are stable. The corrective rotation/translation in figure 3 cannot easily be explained by the mechanical design of the scanner, but it is interesting to notice that the most abrupt variations occur between the camera positions

$\alpha \simeq 45$ and $\alpha \simeq 55$. This is close to the position ($\alpha = 48$) where the detector is vertical and moves upward, back towards the starting position $\alpha = 1$ where the detector is horizontal and at the top of its orbit. Position ($\alpha = 48$) is therefore the position where we expect the required torque to be maximum.

D. *Measured phantom data*

A home-built hot rod phantom similar to Derenzo's phantom was filled with 5 mCi ^{99m}Tc. The phantom is a cylinder of diameter 40 mm, with rods of length 80 mm and diameters 2 mm, 1.8 mm, 1.6 mm, 1.4 mm, 1.2 mm, and 1.0 mm. In each segment the distance between the centers of two adjacent rods is equal to twice the rod diameter. Projection data were acquired for $M = 64$ angular positions of the camera over 360 degrees, with the two detectors heads equipped with a 1.0 mm pinhole. The projection matrix size was 256×256 with a pixel of 2.4 mm. The initial calibration assuming a perfect circular acquisition was done using Bequé's method, and yielded for the first detector head a focal length $F = 267$ mm and a distance between the pinhole aperture and the axis of rotation $ROR = 33.7$ mm. For the second detector head these parameters were $F = 294$ mm and $ROR = 39.8$ mm. With these parameters and the intrinsic resolution of 3.8 mm for the e.cam detector, the standard approximate expression for the spatial resolution of a pinhole system [12] predicts a resolution of about 1.2 mm. After multiplication by the magnification factor F/ROR, this translates into a resolution of 9.3 mm in the detector, indicating that the detector pixel size of 2.40 mm satisfies the condition for aliasing-free sampling. Figure 4 illustrates the improvement of the fit between the measured and the calculated projections of the sources, achieved by refining the initial calibration. After calibration the data were reconstructed on a 256 x 256 x 256 image matrix with 0.25 mm voxels, using 5 iterations of the OSEM algorithm (16 subsets). Attenuation and scatter were not modelled. The transaxial section of the phantom in figure 5 and the profile in figure 6 illustrate the image improvement achieved with the new calibration method.

IV. CONCLUSION

This paper proposes a new method for the geometric calibration of a high resolution pinhole SPECT camera. Contrary to other techniques previously applied in this field, this calibration does not assume that the motion of the gamma camera can be described by a known parametric "nominal" orbit such as a rotation. The main application therefore is for SPECT systems consisting of large rotating gamma cameras because these systems are the most likely to be subject to non negligible mechanical irregularities. Though this remains to be proven, the new method might also be useful with dedicated stationary micro-SPECT systems when extremely small pinhole apertures are used to achieve sub-millimetric resolution, as in [9]–[11].

Following a general idea that has be exploited in photogrammetry [24], the approach is based on the refinement of an initial parametric calibration. Because this refinement is calculated by linearizing the corrective displacement applied to the camera, the approach is only valid provided the deviation from the initial calibration is small, typically smaller than a few mm translation and a few degrees rotation. A second condition is that the deviations from the ideal nominal orbit be reproducible, so that the corrections calculated from the calibration scan are still applicable to the actual scan of the object under study. Both these requirements turned out to be satisfied with the SPECT system used in section III. With that scanner, reproducible deviations larger than 1 mm translation and 1 degree rotation were observed. Though these deviations could not be detected by visual inspection of the camera during acquisition, their correction using the new method improved the image quality in phantom studies.

A significant advantage of the refinement method is that it can be applied with only three calibration sources. If six or more sources are available, an alternative approach is possible: each camera position can be individually calibrated without using the small rotation approximation [25]–[27], [43]. In principle this should further improve the accuracy, but in practice the small rotation approximation is not likely to be an important limitation because modern SPECT systems have a good mechanical stability and the departure from the nominal motion is usually small. When applicable, the refinement method could also positively impact the stability of the calibration because it automatically integrates the prior knowledge that the intrinsic parameters are constant and that the camera orbit deviates only little from a nominal orbit.

Ideally one would like to calibrate the scanner using the projection data of the object under study. This would eliminate the need for a separate calibration measurement, while at the same time guaranteeing immunity to the possible non-reproducibility of the motion of the camera. Developing such a ”data based” calibration represents a difficult challenge unless the object contains easily and accurately segmentable landmarks or additional calibration sources are placed besides the object [39], [41]. The perturbative approach in this paper might offer a promising solution to this problem by reducing the task to that of estimating a small displacement of the detector. This will be the goal of further work.

V. ACKNOWLEDGMENTS

This work was partly supported by a SBO grant of the Instituut voor Wetenschap en Technologie Vlaanderen, and by the Inter-University Attraction Poles Programme 6-38 of the Belgian Science Policy. The authors thank Catherine Mennessier (CPE, Lyon) for drawing their attention to reference [24].

REFERENCES

[1] D. A. Weber, M. Ivanovic, D. Franceschi , S. E. Strand, K. Erlandsson, M. Franceschi et al, ”Pinhole SPECT: an approach to in vivo high resolution SPECT imaging in small laboratory animals,” *J. Nucl. Med.*, vol. 35, pp 342-348, 1994.

[2] P. Wanet and A. Sand, ”Correction of center of rotation in pinhole tomography,” *Eur. J. Nucl. Med.*, vol. 25, pp. PS-646, 1998.

[3] J. Li, R. J. Jaszczak, H. Wang, G. T. Gullberg, K. L. Greer and R. E. Coleman, ”Determination of both mechanical and electronic shifts in cone-beam SPECT,” *Phys. Med. Biol.*, vol. 38, pp. 743-54, 1993.

[4] J. Li, R. J. Jaszczak, and R. E. Coleman, ”Quantitative small field-of-view pinhole SPECT imaging: initial evaluation,” *IEEE Trans. Nucl. Sci.*, vol. 42, pp. 1109-1113, 1995.

[5] F. J. Beekman, D. P. McElroy, F. Berger, S. S. Gambhir, E. J. Hoffman, and S. R. Cherry, ”Towards in vivo nuclear microscopy: iodine-125 imaging in mice using micro-pinholes”, *Eur. J. Nucl. Med.*, vol. 29, pp. 933-938, 2002.

[6] D. P. McElroy, L. R. MacDonald, F. J. Beekman, Y. Wang, B. E. Patt, J. S. Iwanczyk, B. M. W. Tsui, and E. J. Hoffman, ”Performance evaluation of A-SPECT: a high resolution desktop pinhole SPECT system for imaging small animals,” *IEEE Trans. Nucl. Sci.*, vol. 49, pp. 213947, 2002.

[7] N. U. Schramm, G. Ebel, U. Engeland, T. Schurrat, M. Behr, and T. M. Behr, ”High-resolution SPECT using multipinhole collimation,” *IEEE Trans. Nucl. Sci.*, vol. 50, pp. 31520, 2003.

[8] M. A. Kupinski and H. H. Barrett (editors), ”Small-Animal SPECT Imaging”, Springer, 2005.

[9] F. J. Beekman, F. van der Have, B. Vastenhouw, A. J. van der Linden, P. P. van Rijk, J. P. Burbach and M. P. Smidt, ”U-SPECT-I: a novel system for submillimeter-resolution tomography with radiolabeled molecules in mice,” *J. Nucl. Med.*, vol. 46, pp. 1194-1200, 2005.

[10] T. Funk, P. Després, W. C. Barber, K. S. Shah and B. H. Hasegawa, ”A multipinhole small animal SPECT system with submillimeter spatial resolution,”, *Med. Phys.*, vol. 33, pp. 1259-68, 2006.

[11] S. Walrand, F. Jamar, M. de Jong, S. Pauwels, ”Evaluation of Novel Whole-Body High-Resolution Rodent SPECT (Linoview) Based on Direct Acquisition of Linogram Projections,” *J. Nucl. Med.*, vol. 46, pp. 1872-80, 2005.

[12] S. R. Meikle, P. Kench, M. Kassiou, and R. B. Banati, ”Small animal SPECT and its place in the matrix of molecular imaging technologies,” *Phys. Med. Biol.*, vol. 50, pp. R45-R61, 2005.

[13] L. R. Furenlid, D. W. Wilson, Y-C. Chen, H. Kim, P. J. Pietraski, M. J. Crawford, and H. H. Barrett, ”FastSPECT II: a second generation high-resolution dynamic SPECT imager,” *IEEE Trans. Nucl. Sc.*, vol. 51, pp. 6315, 2004.

[14] Y-C. Chen, L. R. Furenlid, D. W. Wilson, and H. H. Barrett, ”Calibration of scintillation cameras and pinhole SPECT imaging systems,” in ”Small-Animal SPECT Imaging,” M. A. Kupinski and H. H. Barrett eds, Springer, pp. 195-202, 2005.

[15] F. van der Have, B. Vastenhouw, M. Rentmeester, F.J. Beekman, ”System Calibration and Statistical Image Reconstruction for Sub-mm Stationary Pinhole SPECT,” in: Conference Record of IEEE 2005 Nuclear Science Symposium and Medical Imaging Conference, 2005, pp. M11-291.

[16] M. F. Smith and R. J. Jaszczak, ”An analytic model of pinhole aperture penetration for 3D pinhole SPECT image reconstruction”, *Phys. Med. Biol.*, vol. 43, pp. 761-775, 1998.1

[17] S. D. Metzler, J. E. Bowsher, K. L. Greer, and R. J. Jaszczak, ”Analytic determination of the pinhole collimator's point-spread function and RMS resolution with penetration”, *IEEE Trans. Med. Imag.*, vol. 21, pp. 878-887, 2002.

[18] M. Gieles, H. de Jong, and F. Beekman, ”Monte-Carlo simulations of pinhole imaging accelerated by kernel-based forced detection,” *Phys. Med. Biol.*, vol. 47, pp. 1853-1867, 2002.

[19] G. T. Gullberg, B. M. W. Tsui, C. R. Crawford, J. G. Ballard, and J. T. Hagius, Estimation of geometrical parameters and collimator evaluation for cone beam tomography, *Med. Phys.*, vol. 17, pp. 264-272, 1990.

[20] P. Rizo, P. Grangeat, and R. Guillemaud R, ”Geometric calibration method for multiple-head cone-beam SPECT system,” *IEEE Trans. Nucl. Sc.*, vol. 41, pp. 2748-2757, 1994.

[21] A. Rougée, C. Picard, C. Ponchut, and Y. Trousset, Geometrical calibration of x-ray imaging chains for three-dimensional reconstruction, *Comput. Med. Imaging Graph.*, vol. 17, pp. 295-300, 1993.

[22] L. von Smekal, M. Kachelriess, E. Stepina and W. A. Kalender, ”Geometric misalignment and calibration in cone-beam tomography,”, *Med. Phys.*, vol. 31, pp. 3242-3266, 2004.

[23] J. Mundy and R. Hartley, ”The relationship between photogrammetry and computer vision,” in Proc. SPIE 1993, http://www.syseng.anu.edu.au/ hartley/My-Papers.html, 1993.

[24] B. Triggs, P. McLauchlan, R. Hartley, and A. Fitzgibbon, ”Bundle Adjustment – A Modern Synthesis,” in ”Vision Algorithms: Theory and Practice,” eds. B. Triggs, A. Zisserman and R. Szeliski, *Lecture Notes in Computer Science*, vol. 1883, pp. 298-372, Springer-Verlag, 2000.

[25] M. Karolczak, S. Schaller, K. Engelke, A. Lutz, U. Taubenreuther, K. Wiesent, and W. A. Kalender, ”Implementation of a cone-beam algorithm for single-circle source orbit with embedded misalignment correction using homogeneous coordinates,” *Med. Phys.*, vol. 28, pp. 2050-2069, 2001.

[26] K. Wiesent, K. Barth, N. Navab, T. Brunner, and W. Seissler, ”Enhanced 3D-reconstruction algorithms for C-arm based interventional procedures,” in Proceedings of the 1999 International Meeting on Fully 3D Image Reconstruction, pp. 167-170, 1999.

[27] K. Wiesent, K. Barth, N. Navab, P. Durlak, T. Brunner, O. Schuetz, and W. Seissler, ”Enhanced 3D-reconstruction algorithm for C-arm systems suitable for interventional procedures,” *IEEE Trans. Med. Imag.*, vol. 19, pp. 391-403, 2000.

[28] N. K. Strobel, B. Heigl, T. M. Brunner, O. Schuetz, M. M. Mitschke, K. Wiesent, and T. Mertelmeyer, ”Improving 3D image quality of x-ray C-arm imaging systems by using properly designed pose determination systems for calibration,” in *Proc. SPIE Medical Imaging* vol. 5030, pp. 943-954, 2003.

[29] Y-L. Hsieh, G.L. Zeng, G.T. Gullberg, H.T. Morgan, ”A method for estimating the parameters of a fan-beam and cone-beam SPECT system using five point sources”, *J. Nucl. Med.*, vol. 34, no. 5, pp. 191, 1993.

[30] Y-L. Hsieh, G.L. Zeng, G.T. Gullberg, ”Electronic Calibration of Single Photon Emission Computed Tomography Camera”, U.S. Patent No. 5,481,115, 1996.

[31] Y-L. Hsieh, G.L. Zeng, and G.T. Gullberg, ”Estimation of geometric parameters for cone beam geometry”, in: records of the 1997 International Meeting on Fully Three-Dimensional Image Reconstruction in Radiology and Nuclear Medicine, pp. 150-3.

[32] D. Bequé, J. Nuyts, G. Bormans, P. Suetens, and P. Dupont, ”Characterization of pinhole SPECT acquisition geometry,” *IEEE Trans. Med. Imag.*, vol. 22, pp. 599-612, 2003.

[33] F. Noo, R. Clackdoyle, C. Mennessier, T. A. White, and T. J. Roney, ”Analytic method based on identification of ellipse parameters for scanner calibration in cone-beam tomography,” *Phys. Med. Biol.*, vol. 45, pp. 3489- 3508, 2000.

[34] Y. Wang, B.M.W. Tsui, E.C. Frey, ”Theoretical analysis of conditions for unique solutions in geometric calibrations for cone-beam and pinhole tomography,” in: Conference Record of IEEE 2005 Nuclear Science Symposium and Medical Imaging Conference, 2005, pp. M11-282.

[35] S. D. Metzler, K. L. Greer, and R. J. Jaszczak, ”Determination of mechanical and electronic shifts for pinhole SPECT using a single point source,” *IEEE Trans. Med. Imag.*, vol. 24, pp. 361-370, 2005.

[36] S. D. Metzler, R. J. Jaszczak, N. H. Patil, S. Vemulapalli, G. Akabani, and B. B. Chin, ”Molecular imaging of small animals with a triple-head SPECT system using pinhole collimation,” *IEEE Trans. Med. Imag.*, vol. 24, pp. 853-862, 2005.

[37] Y. Wang and B. M. W. Tsui, ”Pinhole SPECT with different data acquisition geometries: usefulness of unified projection operators in homogeneous coordinates” *IEEE Trans. Med. Imag.*, vol. 26, pp. 298-308, 2007.

[38] D. Bequé, J. Nuyts, P. Suetens, G. Bormans, ”Optimization of geometrical calibration in pinhole SPECT,” *IEEE Trans. Med. Imag.*, vol. 24, pp. 180-190, 2005.

[39] F. P. DiFilippo and M. J. Riffe, ”Accuracy of auto-calibration for pinhole micro-SPECT,” in: Conference Record of IEEE 2005 Nuclear Science Symposium and Medical Imaging Conference, 2005, pp. M03-286.

[40] S. D. Metzler, R. J. Jaszczak, K. L. Greer, and J. E. Bowsher, ”Angular-Dependent Axial-Shift Correction for Pinhole SPECT,” in: Conference Record of IEEE 2005 Nuclear Science Symposium and Medical Imaging Conference, 2005, pp. M11-282.

[41] F. P. DiFilippo, M. J. Riffe, K. M. Harsch, N. P. McCabe, and H. D. Heston, ”Detached multipinhole small animal SPECT device with real-time calibration,” *IEEE Trans. Nucl. Sc.*, vol. 53, pp. 2605-2612, 2006.

[42] D. Bequé, C. Vanhove, A. Andreyev, J. Nuyts, and M. Defrise, ”Correction for imperfect camera motion and resolution recovery in pinhole SPECT,” in: Conference Record of IEEE 2004 Nuclear Science Symposium and Medical Imaging Conference, pp. M11-291, 2004.

[43] Y. Cho, D. J. Moseley, J. H. Siewerdsen, and D. A. Jaffray, ”Accurate technique for complete geometric calibration of cone-beam computed tomography systems,” *Med. Phys.*, vol. 32, pp. 968-983, 2005.

[44] A. Sommerfeld, ”Mechanics of deformable bodies,” Lectures on theoretical physics II, Academic Press, New York (page 3), 1950.

[45] H. H. Barrett and K. J. Meyers, ”Foundations of Image Science,” Wiley (chapter I), 2004.

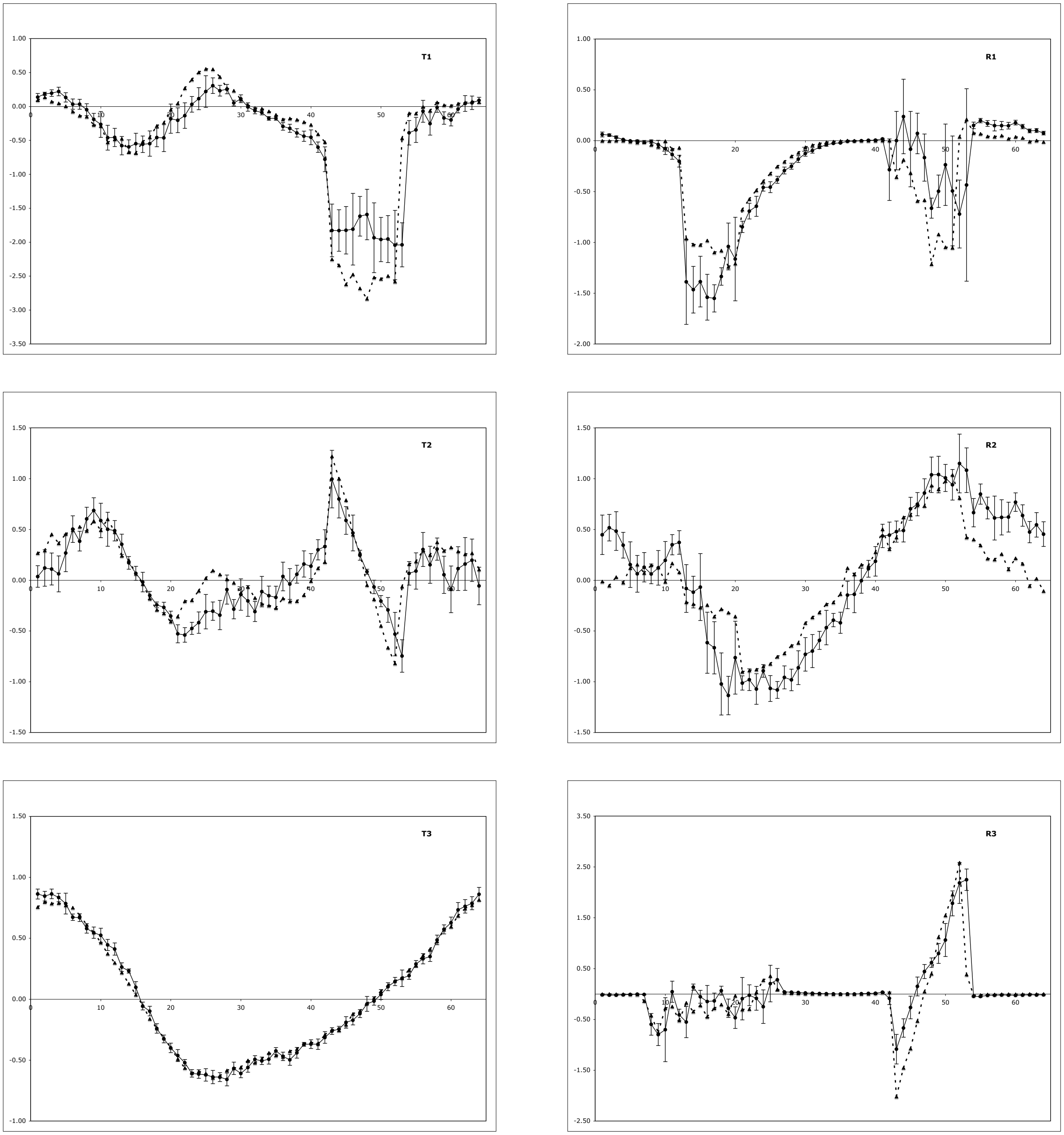

Fig. 3. The three components of the translation vector $\vec{t}_\alpha$ (left column, vertical axis in mm) and of the rotation vector $\vec{\theta}_\alpha$ (right column, vertical axis in degree) for the 64 positions of the camera. These parameters are calculated from a 15 min calibration scan and parametrize the rigid body transformation to be applied to the camera for each position determined by an initial calibration based on a perfect rotation. The x, y and z components are shown on the first, second and third row respectively, with the $z-$axis along the approximate rotation axis of the scanner. The two curves correspond to two sets of 10 successive calibration scans taken on December 15, 2006 (circles with full line) and on January 12, 2007 (triangles with dashed line). Error bars are shown only for the first set, and are calculated as the standard deviation of the 10 calibration scans.

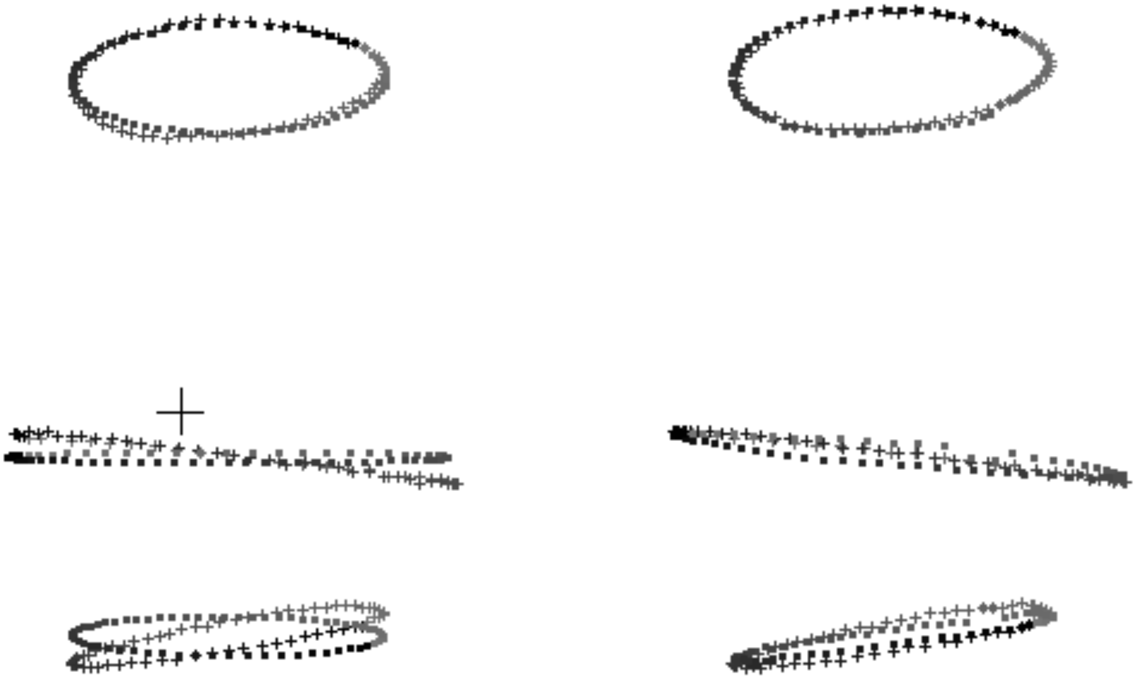

Fig. 4. The detector plane with the u (horizontal axis) and v (vertical axis) coordinates of the three calibration sources for the $\alpha = 1, \cdots, 64$ positions of the first detector head of the camera. Measured and calculated projections are shown respectively by crosses and by filled squares. Left: the calculated projections are obtained using a calibration that assumes a perfect circular orbit of the camera. Right: the calculated projections are obtained using the refined calibration.

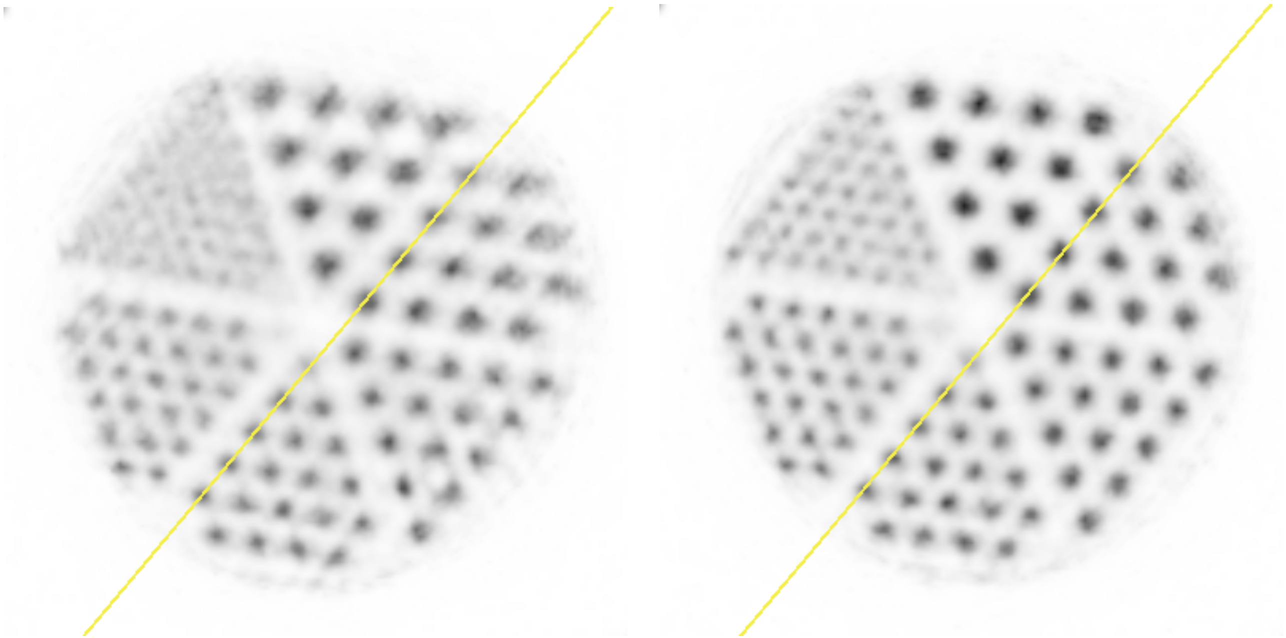

Fig. 5. Reconstructed transaxial section of the micro Derenzo phantom, summed over an axial thickness of 1 cm. The rod diameter in the six segments are respectively 2 mm, 1.8 mm, 1.6 mm, 1.4 mm, 1.2 mm, and 1.0 mm. Left: reconstruction after a calibration assuming a perfect circular orbit of the camera. Right: reconstruction using the refined calibration parameters. The profile in figure 6 is taken along the oblique line.

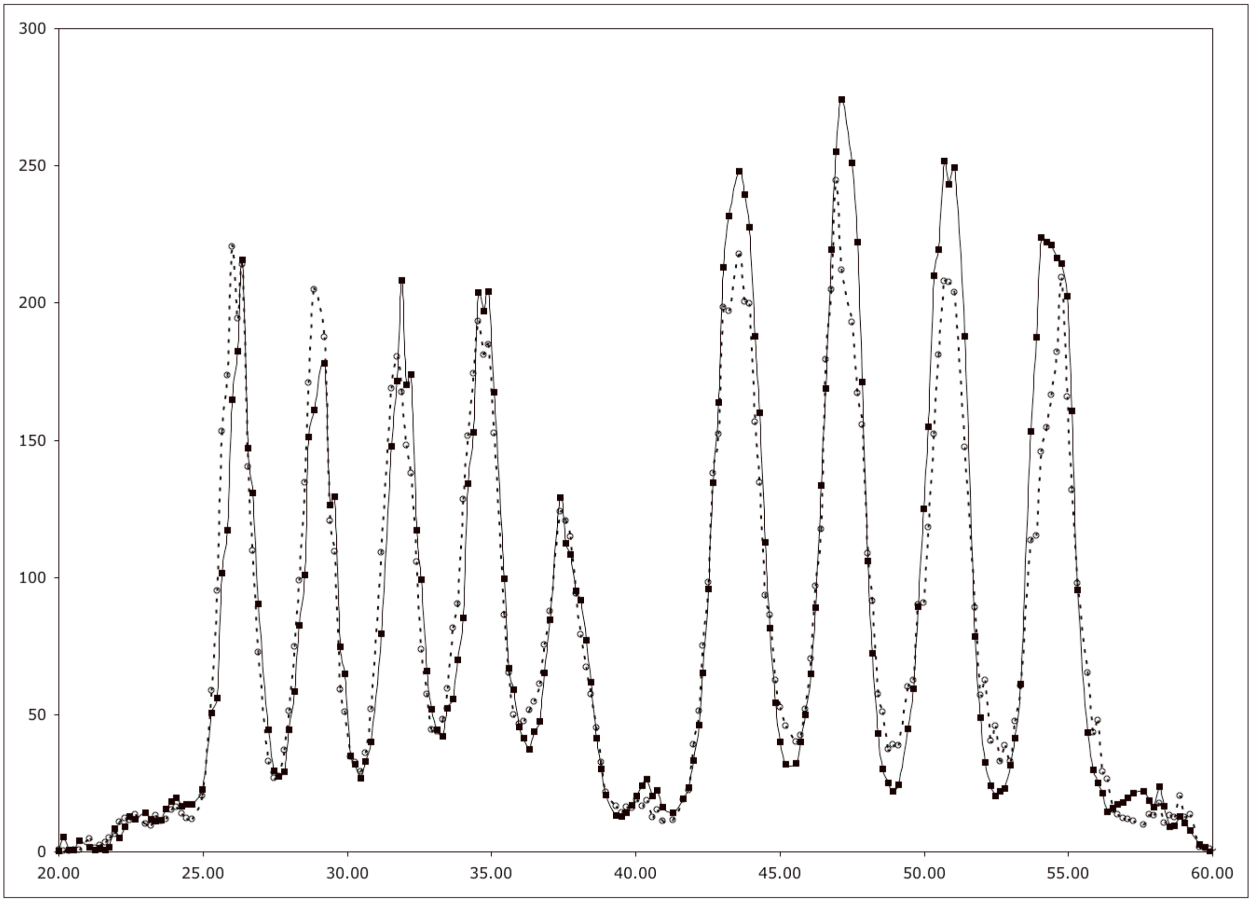

Fig. 6. Profile through the reconstructed transaxial section of the micro Derenzo phantom, summed over an axial thickness of 1 cm. Dashed with open circles: reconstruction after a calibration assuming a perfect circular orbit of the camera. Full line with filled squares: reconstruction using the refined calibration parameters. The horizontal axis is in mm. The profile is along the oblique line shown in figure 5.